Computer Modeling in Engineering & Sciences

Tech Science Press

https://doi.org/10.32604/cmes.2026.087824

ARTICLE

Numerical Investigation of the Interaction between Cavitation and Air Bubbles in a Tube

Shiyu Liu[1], **Bingqi Wang**[1], **Jiangshan Jin**[2,*], **Jia Liu**[2], **Deyu Wang**[2] **and Pu Cui**[1,3,*]

[1]Sanya Nanhai Innovation and Development Base of Harbin Engineering University, Sanya, China
[2]National Key Laboratory of Marine Engine Science and Technology, Shanghai, China
[3]College of Shipbuilding Engineering, Harbin Engineering University, Harbin, China

*Corresponding Authors: Jiangshan Jin. Email: jinjiangshan@smderi.cn; Pu Cui. Email: cuipu@hrbeu.edu.cn

Received: 23 June 2026; Accepted: 07 August 2026; Published: 28 August 2026

ABSTRACT: The interaction between a cavitation bubble and an air bubble inside a rigid tube is numerically investigated using a compressible volume-of-fluid (VoF) method. Two dimensionless parameters are introduced: the spacing ratio γ and the size ratio η. The simulation results show that the spherical pressure wave generated by the expansion of the cavitation bubble propagates outward and reflects at both the tube wall and the air-liquid interface, creating a complex local pressure field. Based on the jet morphology, three typical regimes are identified, namely reverse jets, opposed jets, and co-directional jets; a phase diagram is constructed to delineate the transition patterns among these regimes in the (γ, η) parameter space. The jet direction is primarily influenced by two driving effects, i.e., the pressure impulse and the fluid-flow driving effect. This study contributes to a deeper understanding of cavitation-air bubble interaction under wall confinement and may offer useful insights for flow control in microfluidic and other confined liquid systems.

KEYWORDS: Cavitation bubble; air bubble; VoF; jet formation

1 Introduction

Cavitation bubble dynamics have been extensively studied in both mechanism analysis and engineering applications. When a cavitation bubble oscillates near a boundary, including rigid [1,2], elastic [3,4], free-surfaces [5–7], and composite boundaries [8–10], complex phenomena such as jet formation and material erosion emerge [11,12]. However, in many practical scenarios, cavitation bubbles do not exist in isolation. The coupling among multiple bubbles is common. The air-liquid interface can reflect and absorb pressure waves, thereby modifying the evolution of adjacent cavitation bubbles and their directional jet behavior [13,14]. In studies of cavitation bubble pair interaction, the coupling between cavitation bubbles is mainly affected by geometric parameters and phase difference. These factors determine bubble deformation, jet direction, and pressure distribution. When two bubbles oscillate in phase, they attract each other during collapse. When two bubbles oscillate in opposite phase, they generate directional jets (pointing toward neighboring bubbles or boundaries), asymmetric collapse, and ring jets, which together become an efficient means of fluid transport [15,16]. In contrast, the interaction between a cavitation bubble and an air bubble is not affected by phase difference [17,18]. The air bubble has a compressible air-liquid interface that can reflect and absorb shock waves [19]. This property influences the oscillation and jet direction of the cavitation bubble.

By adjusting the geometric confinement and flow conditions between bubbles, the jet shape and velocity can be effectively controlled, providing a new idea for flow regulation in confined spaces.

Compared with cavitation in the free field, bubble dynamics in a confined geometry exhibit more complex shape evolution and jets in different directions. In practice, the coexistence of cavitation bubbles with pre-existing air bubbles is common in confined geometries such as tubes and microchannels. In circular tubes, the wall imposes strong constraints on radial expansion, leading to elongated bubble shapes, annular jets, and reflected pressure waves [20]. Such confined bubble interactions are of interest in fields such as hydraulic engineering [21], microfluidics [22], and biomedical processes [23]. Previous studies have focused primarily on single cavitation bubbles inside tubes, or on the interaction between two cavitation bubbles in free fields. Only a few investigations have considered the combined effects of an air bubble and a tube wall on cavitation bubble dynamics [24,25]. Recent studies have begun to explore this interaction in unbounded domains [14,26], but the effect of wall confinement remains largely unexplored, particularly within a tube. Consequently, the underlying mechanisms governing pressure attenuation, jet direction, and bubble-bubble energy transfer in such confined tubes remain elusive.

In this paper, we investigate the cavitation–air bubble interaction inside a rigid circular tube using a compressible volume-of-fluid (VoF) method. Two dimensionless parameters are considered: the spacing ratio $\gamma = L/R_m$ and the size ratio $\eta = R_m/R_a$, where L is the distance from the center of the cavitation bubble to the wall surface of the air bubble, R_m is the equivalent maximum radius of the cavitation bubble, and R_a is the initial radius of the air bubble. The simulations reveal that the air bubble reduces the wall pressure amplitude and redirects the cavitation bubble jet. Based on the parametric study, three distinct jetting regimes are identified, and a phase diagram is constructed to map the transitions. The paper is organized as follows. Section 2 describes the numerical methodology and validation. Section 3 presents the results on wall pressure dynamics and bubble–bubble interaction. Section 4 concludes the study.

2 Numerical Methods

2.1 Numerical Methodology

Numerical simulations in this study are performed within the OpenFOAM framework [27], employing a compressible Volume-of-Fluid (VoF) solver that has been validated against experiments for cavitation bubble dynamics [28].

The gas and liquid phases are both treated as compressible and immiscible, with no heat or mass transfer assumed across their interface [29]. The adiabatic assumption is justified by the thermal Péclet number $\sim O(10^4)$, indicating that convection dominates over diffusion during the short first collapse [30]. Interfacial heat and mass transfer are therefore omitted, though they could play a role over longer timescales. Under these conditions, the flow field is governed by the compressible Navier-Stokes equations, comprising the continuity and momentum conservation laws:

$$\frac{\partial \rho}{\partial t} + \nabla \cdot (\rho \boldsymbol{u}) = 0, \tag{1}$$

$$\frac{\partial \rho \boldsymbol{u}}{\partial t} + \nabla \cdot (\rho \boldsymbol{u}\boldsymbol{u}) = -\nabla p + \nabla \cdot \boldsymbol{\tau} + \boldsymbol{f_\delta}, \tag{2}$$

where ρ, $\boldsymbol{u}$, t, and p denote the density, velocity, time, and pressure, respectively. The viscous stress tensor is expressed as $\boldsymbol{\tau} = \mu[\nabla \boldsymbol{u} + \nabla \boldsymbol{u}^T - \frac{2}{3}(\nabla \cdot \boldsymbol{u})\boldsymbol{I}]$, where μ is the dynamic viscosity and $\boldsymbol{I}$ is the identity tensor. The term $\boldsymbol{f_\delta}$ represents the surface tension modeled using the continuous surface force (CSF) [31] method.

A two-phase interface capturing approach is adopted, in which the evolution of the gas-liquid boundary is tracked by solving a transport equation for the volume fraction α:

$$\frac{\partial \alpha}{\partial t} + \nabla \cdot (\alpha \boldsymbol{U}) + \nabla \cdot [\alpha(1-\alpha)\boldsymbol{U_r}] = \alpha(1-\alpha)\left(\frac{\psi_g}{\rho_g} - \frac{\psi_l}{\rho_l}\right)\frac{Dp}{Dt} + \alpha \nabla \cdot \boldsymbol{U}, \tag{3}$$

where $\psi = D\rho/Dp$ represents the fluid compressibility derived from the respective equation of state (EOS). The subscripts l and g correspond to the liquid and gas phases, respectively. Relative velocity $\boldsymbol{U_r}$ serves as an artificial compression term that preserves a sharp interface between the two phases.

The cavitation bubble is initialised as a spherical volume of gas at high pressure. This modeling approach has been widely validated for reproducing the first oscillation cycle of a cavitation bubble [32]. Initially, the air bubble was built as a steady spherical bubble given by $p_\infty + 2\sigma/R_a$, where σ is the surface tension coefficient. A polytropic equation of state is employed for the gas phase, while the liquid phase is modelled as a compressible Tait fluid. The surrounding flow field was solved simultaneously using the compressible Navier-Stokes equations and the volume-fraction transport equation implemented [27,33] in OpenFOAM.

Time integration was performed using adaptive time-step control based on the Courant number ($Co < 0.1$) to ensure numerical stability. The pressure–velocity coupling was solved using the PIMPLE algorithm with iterative correction. Further details of the numerical implementation can be found in our earlier work [34].

2.2 Numerical Model

As shown in Fig. 1, the domain is simplified. The tube has a radius of R_t, and No-slip conditions are applied at the tube wall. The length of the tube is greater than 80 times its radius. A zero-gradient condition is imposed on pressure and velocity at the remaining boundaries to allow inflow and outflow.

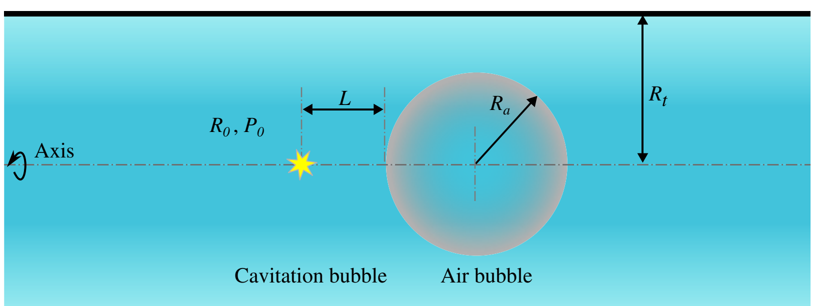

Figure 1: Diagram showing the numerical settings for the cavitation bubble and the air bubble within the tube. The coordinate origin is set at the center of the air bubble.

In the simulations, the initial bubble is assumed to be spherical, with an internal pressure of P_0 = 2500 bar and an initial radius of R_0 = 40 μm. The bubble center is placed on the tube axis. The initial liquid pressure inside the tube is set to P_∞ = 1.013 bar.

We define two dimensionless parameters that characterize the bubble dynamics. Dimensionless distance γ and relative size ratio η,

$$\gamma = \frac{L}{R_m}, \tag{4}$$

$$\eta = \frac{R_m}{R_a} \tag{5}$$

here, L represents the distance from the center of the cavitation bubble to the wall of the air bubble, and R_a is the initial radius of the air bubble; R_m is the equivalent maximum radius of cavitation bubbles.

2.3 Grid Independence Study

In the simulation, to reduce computational cost, the domain is modelled as a wedge with an angle of 2 degrees. Five different meshes were used to carry out a grid independence study. Uniform grids were used in the regions containing the two bubbles, with a gradual transition between them. The size of the grid Δx was successively refined to $7.81, 3.91, 3.13, 1.95$ and 1.56 μm. The temporal evolution of the equivalent radius R of the cavitation bubble is shown in Fig. 2. The bubble radius is calculated as $R = \left(\frac{3V}{4\pi}\right)^{1/3}$, where V denotes the bubble volume. When the grid size Δx is reduced below 1.95 μm, further refinement exerts a negligible influence on the calculated bubble radius. Thus, a grid spacing of $\Delta x = 1.95$ μm was adopted for all subsequent simulations.

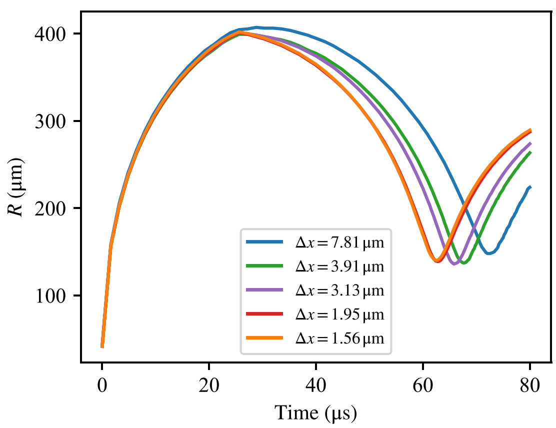

Figure 2: Grid independence study of cavitation bubble radius evolution with varying mesh resolution. Here, $\gamma = 1.25,\ \eta = 0.80$.

2.4 Experimental Verification

We conducted experiments on a single cavitation bubble confined within a rigid circular tube to benchmark the numerical method under the same geometric and initial conditions used in the simulations. Fig. 3 compares the simulated bubble shapes with the experimental images at several representative time instants. As shown in Fig. 3, the simulation results agree well with the experiments in terms of bubble morphology, demonstrating the capability of the compressible VoF method to reproduce the essential physics of cavitation bubble dynamics under wall confinement.

3 Results and Discussion

3.1 Wall Pressure Dynamics

3.1.1 Spatiotemporal Evolution of the Pressure Field

The characteristics of the flow field during the initial bubble growth are first described. Fig. 4 illustrates the pressure distribution and numerical Schlieren visualization for the case of $\gamma = 0.75,\ \eta = 2.00$ and $R_t = 500$ μm. The rapid evolution is captured in Fig. 4 inside the circular tube during the initial phase of cavitation bubble expansion. The schlieren value was calculated as $\exp(-k|\nabla p|/max|\nabla p|)$, where k is a free parameter. As shown in Fig. 4a, a spherical pressure wave is generated during the early stage of cavitation bubble expansion and propagates outward. As the pressure wave approaches the tube wall, the wall pressure reaches its maximum of approximately 230 bar at t = 0.33 µs, see Fig. 4b. Subsequently, the pressure wave is reflected by the wall, and the peak pressure begins to decay, as two symmetric pressure peaks are formed along the wall, as illustrated in Fig. 4c. As the pressure wave continues to propagate (see Fig. 4d), the reflected pressure waves meet each other near the cavitation bubble, producing two localized high-pressure regions. This asymmetric pressure distribution has distinct consequences. On the left side of the cavitation bubble, the pressure wave continues to propagate outward along the tube axis. However, the localized high pressure on the side facing the cavitation bubble suppresses its radial expansion on that side, leading to an asymmetric bubble deformation during expansion and initiating a non-spherical collapse toward the high-pressure region. This asymmetry subsequently leads to a non-spherical bubble collapse. Fig. 4d shows that the wall pressure on the right side of the cavitation bubble is lower than that on the left side during outward pressure wave propagation. This indicates that the presence of the air bubble causes a non-uniform pressure distribution along the wall.

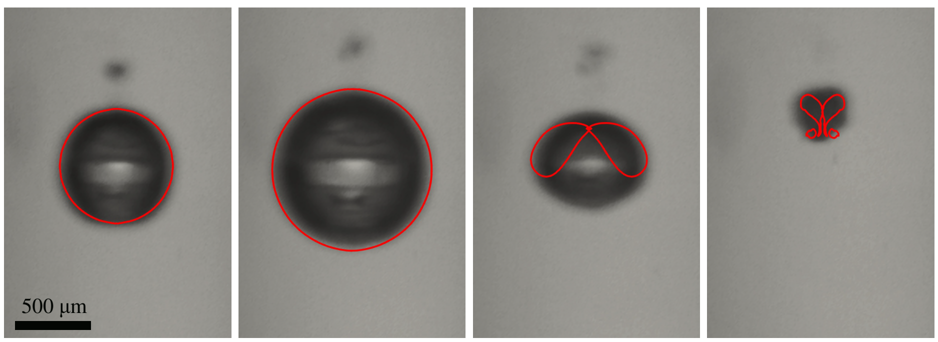

Figure 3: Comparison of experimental images with simulated bubble contours (red). The times are 20, 60, 100, and 120 µs, respectively. The experimental images were captured by a high-speed camera with 50 kfps and an exposure time of 1 µs. The scale bar represents 500 µm.

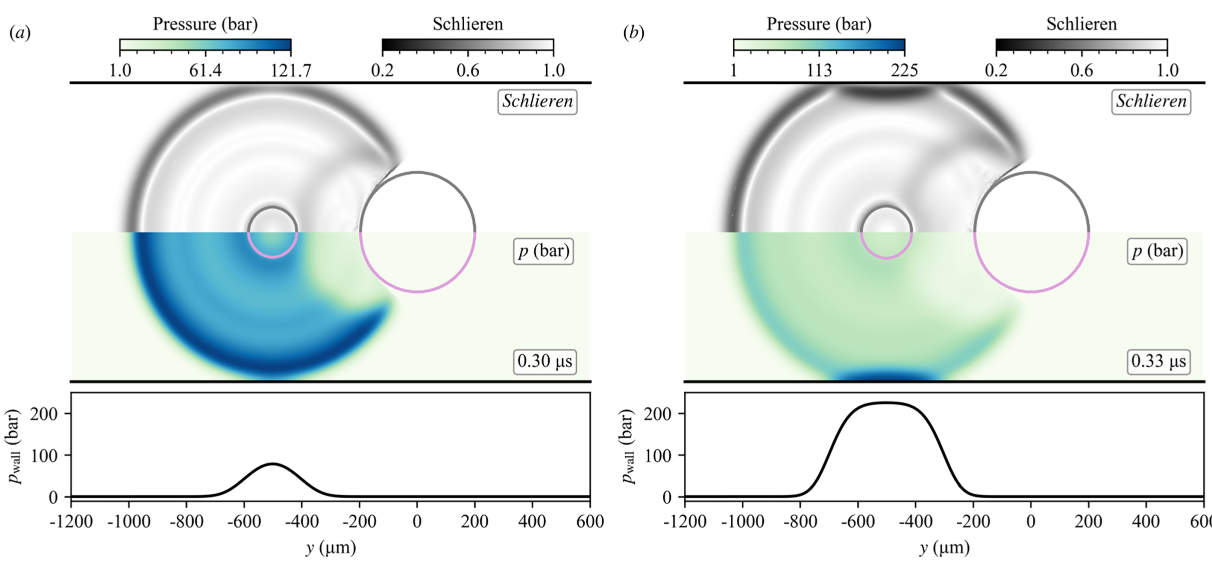

Figure 4: (Continued)

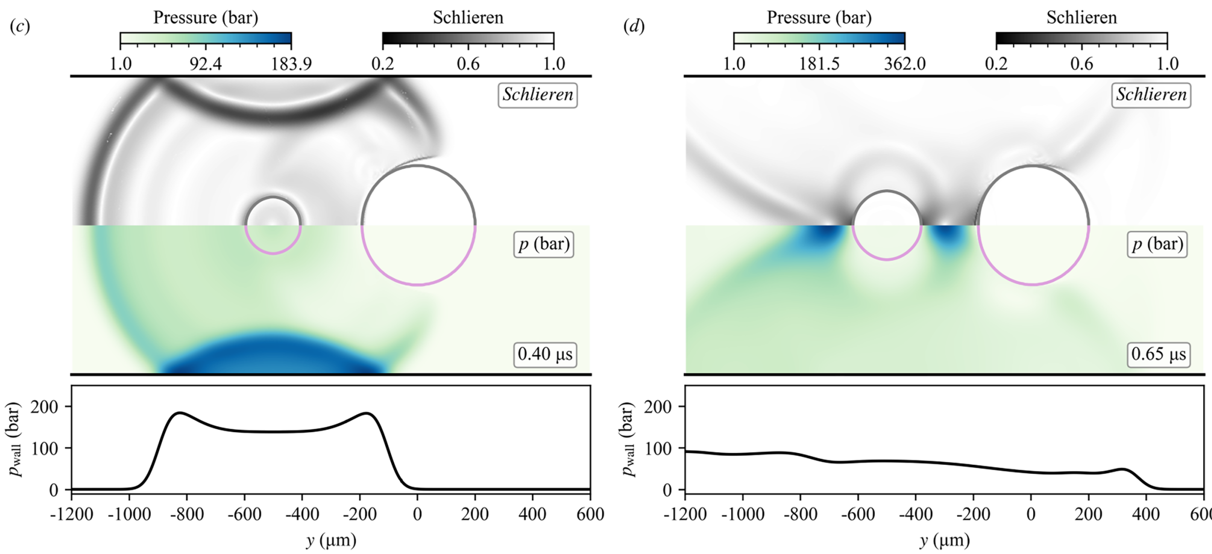

Figure 4: The pressure distribution and numerical Schlieren visualization at different time instants (**a**)–(**d**) for the case of γ = 0.75, η = 2.00 and R_t = 500 μm. Purple and grey contours indicate the gas-liquid interfaces. The lower half of each panel presents the pressure field, and the upper half shows the numerical Schlieren image. At the bottom of the flow field, the wall pressure was plotted along the axial direction y. The coordinate origin is set at the center of the air bubble. The positive y-axis points towards the bubble.

3.1.2 Effect of Dimensionless Parameters (γ, η) under Fixed Tube Radius

The effects of the non-dimensional distance γ and the relative size ratio η on the wall pressure are explored within a fixed radius of the tube with R_t = 500 μm. Fig. 5a illustrates the spatiotemporal evolution of the wall pressure in a circular tube at γ = 1.25 and η = 0.80, as well as Fig. 5b, the peak pressure curves of the wall under different non-dimensional distances γ and various relative size ratios η.

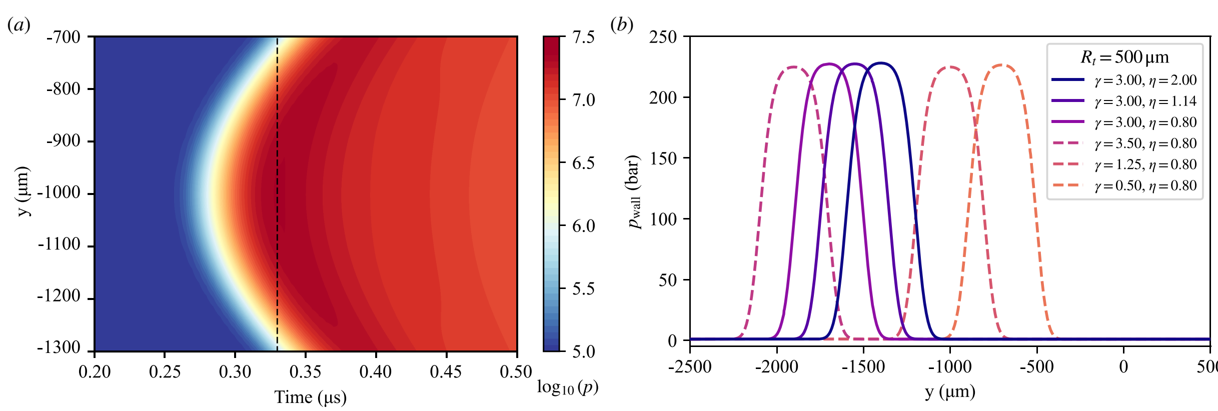

Figure 5: (**a**) The spatiotemporal evolution of wall pressure in a circular tube at γ = 1.25 and η = 0.80 with R_t = 500 μm. The black dotted line represents the moment when the wall pressure reaches its maximum value. (**b**) The wall peak pressure curves at $t \approx 0.33$ μs under different non-dimensional distances γ and various relative size ratios η. The solid line represents the same non-dimensional distance γ, while the dotted line represents the same relative size ratios η. The coordinate origin is set at the center of the air bubble. The positive y-axis points towards the bubble.

As shown in Fig. 4a, a clear pressure front appears around $t \approx 0.30$ μs, the pressure wave propagates nearly spherically. When the pressure wave reaches the tube wall, the wall pressure reaches its maximum at $t \approx 0.33$ μs, approximately 230 bar (see Fig. 4b). The black dotted line represents the moment when the wall pressure reaches its maximum value. In this stage, the pressure wave propagates rapidly with a large gradient. The pressure pulse load applied to the tube wall can cause deformation of the tube wall or even material damage. Fig. 5b shows the maximum pressure of the tube wall distributions under different dimensionless parameters (R_t = 500 μm). Different colors and line styles denote the non-dimensional distance γ and the relative size ratio η. For the same tube radius, the variations in γ and η exert little influence on the pressure amplitude, with the peak pressure remaining around 230 bar. The results show that the influence of the non-dimensional distance γ and the relative size ratio η on the wall pressure amplitude is very small, within the same tube radius.

3.1.3 Effect of Tube Radius R_t on Peak Wall Pressure

Fig. 6 illustrates the spatiotemporal evolution of wall pressure and the corresponding peak pressure profiles under different tube radii for $\gamma = 0.75$ and $\eta = 2.00$. As shown in Fig. 6a, the spatiotemporal evolution of wall pressure is presented for R_t = 300 μm. The pressure wave propagates as a spherical wave, with a clear pressure front appearing at $t \approx 0.16$ μs. Compared with the case of R_t = 500 μm (see Fig. 4), a smaller tube radius results in the pressure wave reaching the tube wall earlier and producing a higher peak wall pressure. At $t \approx 0.19$ μs (marked by the black dashed line), the wall pressure reaches its maximum of approximately 430 bar, revealing a strong pressure effect in the narrow tube. Fig. 6b shows the profiles of the wall pressure peak under identical parameters $\gamma = 0.75$ and $\eta = 2.00$ but with varying tube radii R_t. Different colors represent different radii. In a narrower tube, the pressure wave reaches the tube wall in a shorter time, and the peak pressure amplitude is significantly enhanced. As R_t increases, the pressure peak decreases and occurs later in time. These results indicate that reducing the radius of the tube amplifies the impulsive loading on the wall, which is exacerbated by the risk of cavitation-induced damage to the tube.

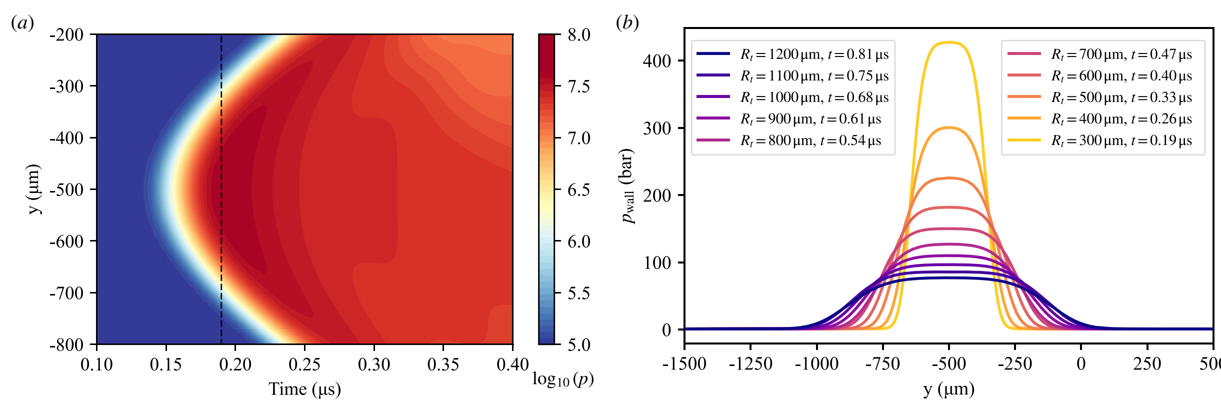

Figure 6: (**a**) The spatiotemporal evolution of wall pressure in a circular tube at $\gamma = 0.75$ and $\eta = 2.00$ with R_t = 300 μm. The black dotted line represents the moment when the wall pressure reaches its maximum value. (**b**) The wall peak pressure curves at $\gamma = 0.75$ and $\eta = 2.00$ under different the radius of the circular tube R_t, ranging from 300 to 1200 μm. The color of the solid line becomes darker as the radius of the circular tube increases. The coordinate origin is set at the center of the air bubble. The positive y-axis points towards the bubble.

3.2 Bubble–Bubble Interaction and Jet Regimes

Having characterized the wall pressure dynamics, we now turn to the interaction between the cavitation bubble and the air bubble, focusing on jet formation regimes.

3.2.1 Effect of Size Ratio η at a Fixed Spacing γ = 3.00

To elucidate the effects of the interplay between a cavitation bubble and an air bubble on the internal flow dynamics, we first consider the case of fixed bubble spacing while varying the size ratio. Fig. 7 illustrates the temporal morphological evolution of a cavitation bubble and an adjacent air bubble inside a rigid circular tube at a fixed non-dimensional distance $\gamma = 3.00$ with varying size ratios ($\eta = 2.00, 1.14$ and 0.80). The cavitation bubble is initially positioned on the left side. At $t = 1.4$ μs, the primary pressure wave induced by the explosive expansion of the cavitation bubble impinges upon the proximal interface of the air bubble. Subsequently, the rapid expansion of the cavitation bubble vigorously squeezes the inter-bubble liquid. Restricted by the rigid tube wall boundary condition, the fluid momentum is restricted from radial expansion. It is channeled predominantly along the axial direction, leading to the development of a forward-directed liquid jet inside the air bubble. For $\eta = 2.00$, the cavitation bubble generates a reverse jet. As η decreases, the volume of the air bubble expands, causing its interface to become significantly flattened. At $\eta = 1.14$, the proximal and distal surfaces of the cavitation bubble contract simultaneously toward its geometric center, exhibiting distinct features of opposed jetting. For a smaller size ratio of $\eta = 0.80$, the collapse of cavitation bubbles generates obvious co-directional jets.

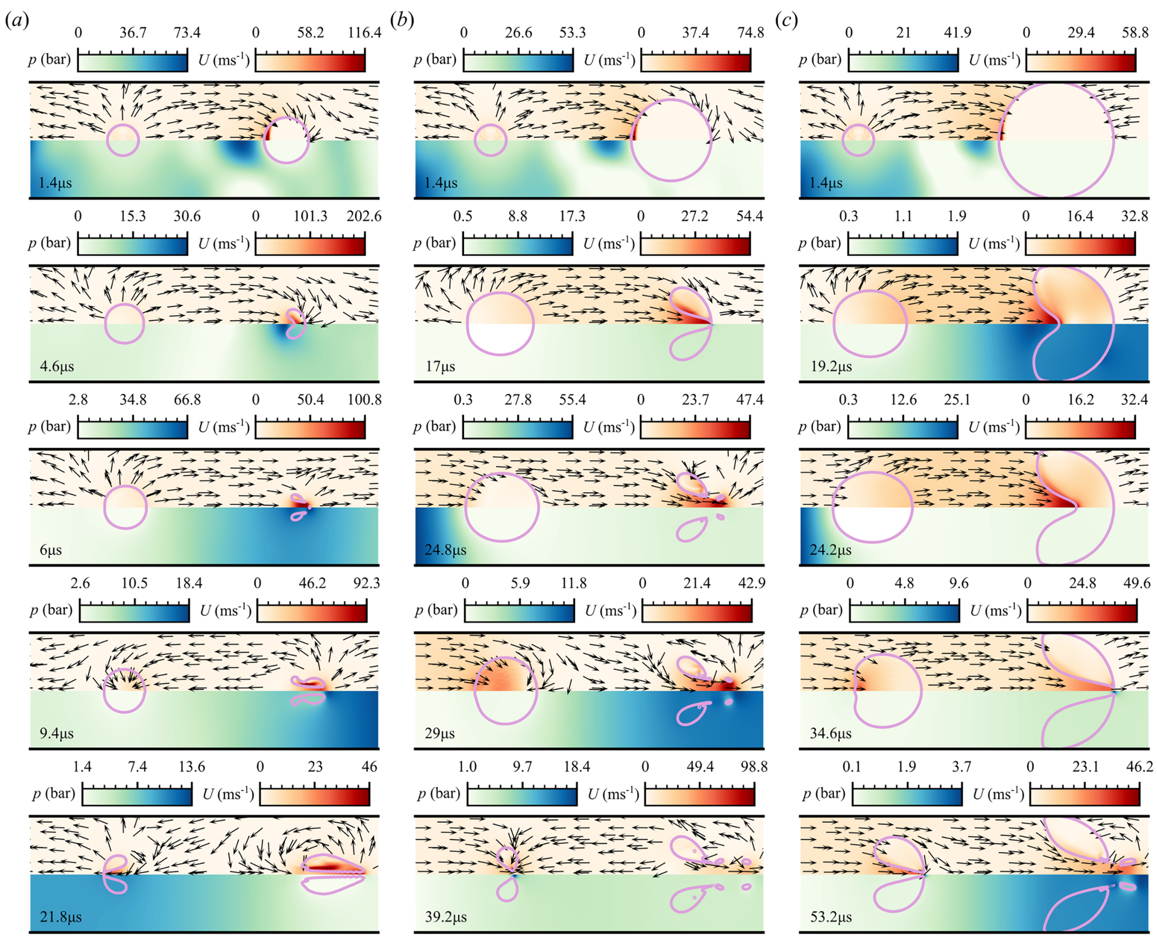

Figure 7: The evolution of bubble shapes as well as pressure and velocity distributions. Purple lines denote bubble interfaces, the pressure (lower halves), and flow fields (upper halves). Magnitudes are color-coded, and arrows indicate flow directions. Color bars indicate pressure (in bar) or velocity magnitude (in ms^{-1}), as labelled. The coordinate origin is set at the center of the air bubble. The positive y-axis points towards the bubble. Each frame is 3 mm wide. (**a**) $\gamma = 3.00$ and $\eta = 2.00$; (**b**) $\gamma = 3.00$ and $\eta = 1.14$; (**c**) $\gamma = 3.00$ and $\eta = 0.80$.

These dynamic trends can be quantitatively evaluated through analysis of bubble trajectories and jet velocities. Fig. 8 further illustrates the influence of the relative size ratio η on bubble morphology and jet velocity at the dimensionless distance γ = 3.00. Specifically, Fig. 8a,b plot the moving trajectories of two representative monitoring points on the air bubble and the cavitation bubble, respectively, along the axis of symmetry (y-axis). At γ = 3.00, the y-direction trajectories of the air bubble exhibit significant variations across different η values. As shown in Fig. 8a, when η = 2.00, the air bubble radius is relatively small. This allows a portion of the pressure wave to bypass it, driving the right side of the air bubble toward its center. The intersection of the two trajectories occurs inside the bubble, indicating severe deformation of the air bubble wall. Conversely, at η = 1.14 and η = 0.80, the left wall of the air bubble moves rapidly toward the right upon the arrival of the pressure wave from the expanding cavitation bubble. As η gradually decreases, the air bubble radius increases, and the position of the air bubble's right wall remains largely unchanged. The two trajectories intersect at the right wall. Turning to the cavitation bubble in Fig. 8b, when η = 2.00, the intersection of its two trajectories appears below the center of the cavitation bubble, indicating that the cavitation bubble is moving away from the air bubble. At η = 1.14, the intersection shifts to near the center of the cavitation bubble, suggesting that both the left and right sides of the cavitation bubble are moving inward toward its center. Finally, at η = 0.80, the intersection occurs above the center of the cavitation bubble, demonstrating that the cavitation bubble is migrating toward the air bubble.

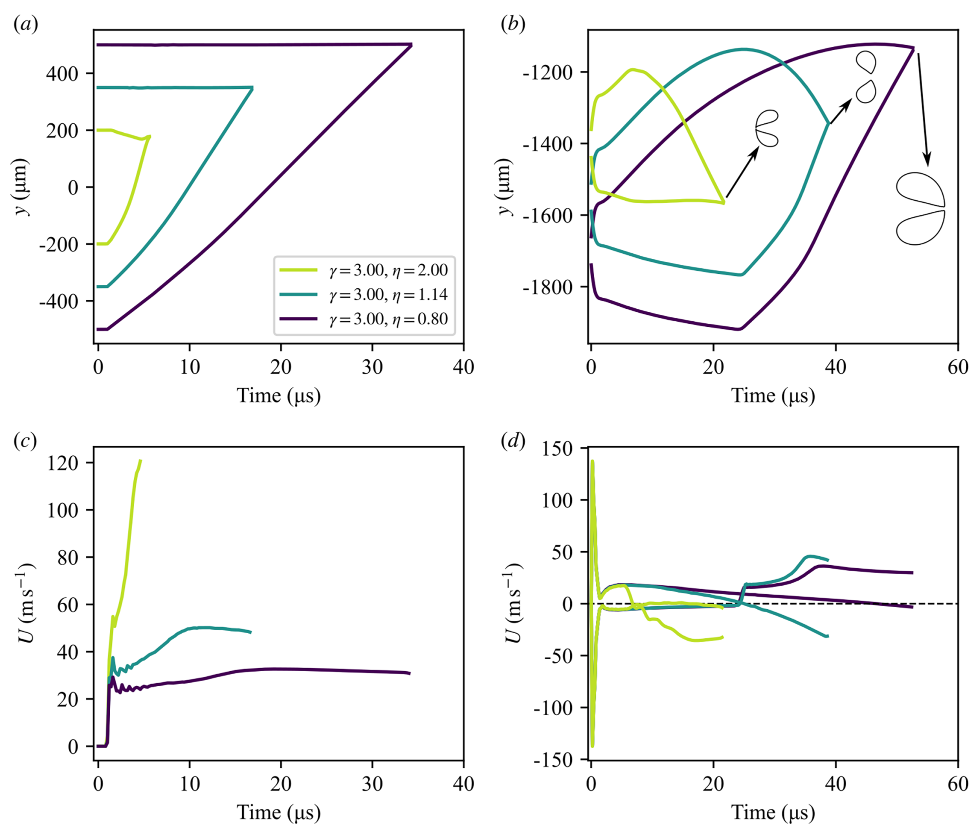

Figure 8: Influence of the relative size ratio η on bubble morphology and jet velocity at the non-dimensional distance γ = 3.00. (**a**) Temporal evolution of the left and right interfaces of the air bubble; (**b**) temporal evolution of the left and right interfaces of the cavitation bubble; (**c**) velocity of the left interface of the air bubble; (**d**) velocity of the left and right interfaces of the cavitation bubble. Different colors represent distinct values of η. The positive y-axis points towards the bubble. Negative velocities indicate leftward motion. The black contours in (**b**) show three representative cavitation-bubble shapes.

Fig. 8c illustrates the velocity-time histories of the left wall of the air bubble under three different conditions, while Fig. 8d plots the corresponding data for the left and right walls of the cavitation bubble, with velocities directed along the positive y-axis defined as positive. For the air bubble at $\eta = 2.00$, the high interfacial curvature strongly focuses the pressure wave toward the central axis, concentrating fluid momentum within a highly localized region. Governed by the Euler equation, $\rho \frac{Du}{Dt} = -\nabla p$, this extreme pressure gradient ∇p drives the initial velocity of the air bubble interface up to 58 m/s. Subsequently, the confinement of the circular tube induces further flow focusing, accelerating the jet to a maximum velocity of 120 m/s as it penetrates the right wall. Similarly, at $\eta = 1.14$ and $\eta = 0.80$, a remarkably brief pressure pulse imparts an initial velocity to the wall, followed by flow focusing that accelerates the jet to its peak velocity before piercing the right wall of the air bubble. Turning to the cavitation bubble dynamics shown in Fig. 8d, the initial surface expansion rates are nearly identical across all three cases; however, their subsequent behaviors diverge. At $\eta = 2.00$, once the cavitation bubble wall velocity drops to zero, the left wall ceases to expand and remains stationary, whereas the right wall's velocity reverses direction to form a leftward jet. At $\eta = 1.14$, after the velocity curves for both sides cross the zero axis, the walls simultaneously contract inward toward the bubble's interior, generating counter-penetrating jets. Finally, at $\eta = 0.80$, the velocity on the left wall of the cavitation bubble reaches zero first, after which the velocities of the left and right interfaces become equal and positive, demonstrating that the right wall continues to expand while a rightward jet forms on the left wall.

3.2.2 Effect of Spacing Ratio γ at a Fixed Size Ratio $\eta = 0.80$

Having examined the role of size ratio, we now turn to the effect of bubble spacing. Fig. 9 illustrates the temporal shape evolution of the cavitation bubble and the air bubble, at a fixed size ratio $\eta = 0.80$ across different dimensionless distances $\gamma = 0.50, 1.25$ and 3.50. Fig. 10 reveals the kinematic characteristics of the interaction between a cavitation bubble and an air bubble in a circular tube.

At $\gamma = 0.50$, the cavitation bubble is near the air bubble, producing strong bubble–bubble coupling. At $t = 0.8$ μs, the shock wave reaches the air bubble interface immediately after cavitation, producing a high initial acceleration and a visible indentation on the air bubble surface. The velocity curve (Fig. 10c) shows that the jet speed reaches a peak of approximately 80 m/s. At $t = 13.2$ μs, the jet penetrates the right boundary of the air bubble, while at $t \approx 13.0$ μs (Fig. 10d), the left side of the cavitation bubble develops a negative velocity, forming an opposed jet directed leftward. The velocity of the jet increases rapidly; by $t = 21.6$ μs, the counter jet penetrates the left wall of the cavitation bubble with a velocity of approximately 130 m/s.

With an intermediate spacing of $\gamma = 1.25$, the interaction between the two bubbles becomes less pronounced. The air bubble jet reaches an initial velocity peak at $t = 1.0$ μs, and the subsequent motion evolves more gradually. At $t = 25.6$ μs, the jet directed to the right penetrates the bubble wall with a velocity of approximately 40 m/s (Fig. 10c). Later, at $t = 50.6$ μs, two opposed jet form within the cavitation bubble and collide in the center, with velocities near 20 m/s.

When the spacing increases further to $\gamma = 3.50$, the bubble interaction weakens considerably. During the early expansion stage, the cavitation bubble remains nearly spherical. At $t = 1.4$ μs, the air–bubble interface reaches a peak velocity of 28 m/s (Fig. 10c). Subsequently, the air bubble jet gradually shifts to the right and penetrates the interface around $t = 35$ μs. Meanwhile, at $t = 24.2$ μs, a jet appears on the left side of the cavitation bubble directed toward the air bubble.

In a circular tube, the collapse and jetting of the cavitation bubble are mainly caused by two driving effects. One is the pressure impulse reflected from the tube wall, which pushes the bubble rightward and promotes a rightward-directed jet. The other is the re-expansion of the air bubble after its right interface is pierced by the jet, which drives the fluid between the bubbles leftward and produces a leftward jet.

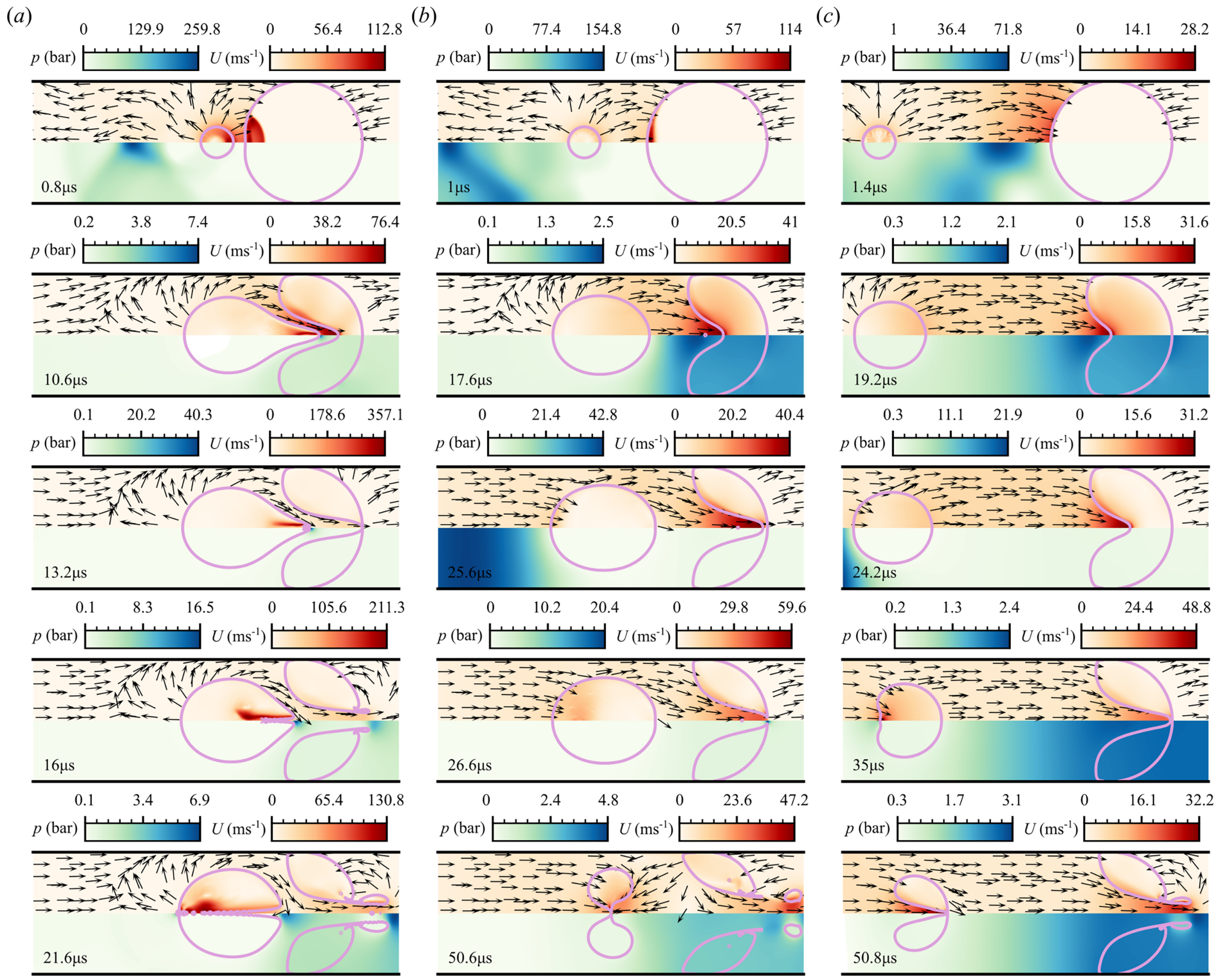

Figure 9: The evolution of bubble shapes as well as pressure and velocity distributions. Purple lines denote bubble interfaces, the pressure (lower halves), and flow fields (upper halves). Magnitudes are color-coded, and arrows indicate flow directions. Color bars indicate pressure (in bar) or velocity magnitude (in ms^{-1}), as labelled. The coordinate origin is set at the center of the air bubble. The positive y-axis points towards the bubble. Each frame is 3 mm wide. (**a**) $\gamma = 0.50$ and $\eta = 0.80$; (**b**) $\gamma = 1.25$ and $\eta = 0.80$; (**c**) $\gamma = 3.50$ and $\eta = 0.80$.

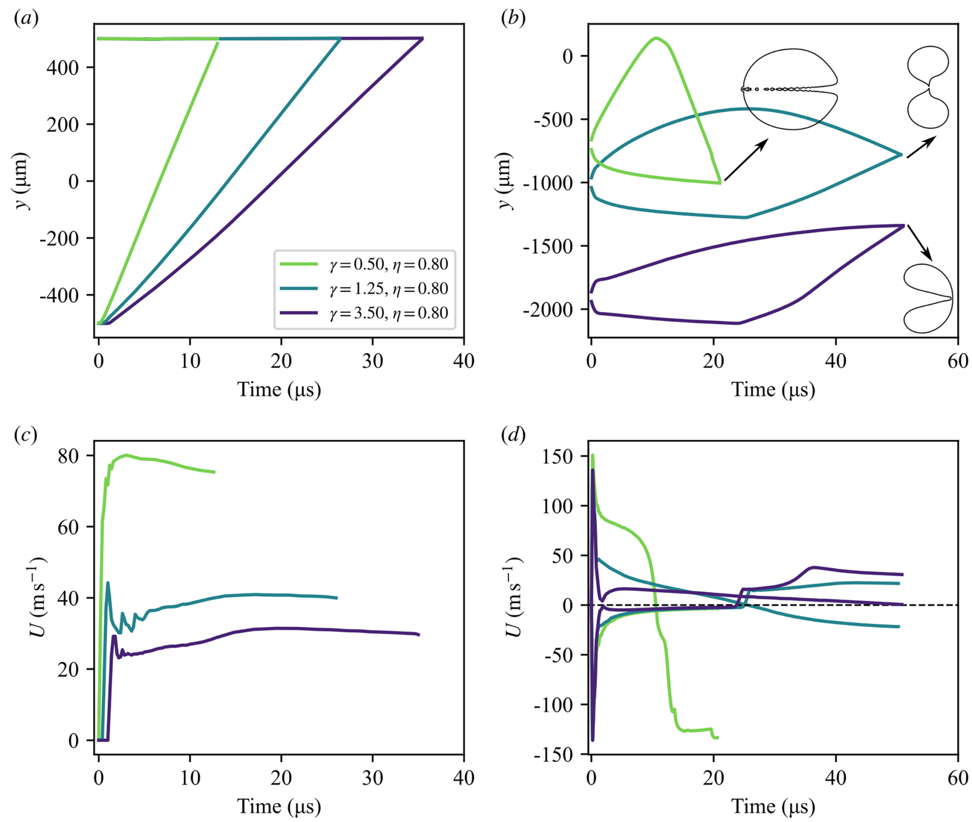

Figure 10: Influence of the non-dimensional distance γ on bubble morphology and jet velocity at the relative size ratio η = 0.80. (**a**) Temporal evolution of the left and right interfaces of the air bubble; (**b**) temporal evolution of the left and right interfaces of the cavitation bubble; (**c**) velocity of the left interface of the air bubble; (**d**) velocity of the left and right interfaces of the cavitation bubble. Different colors represent distinct values of γ. The positive y-axis points towards the bubble. Negative velocities indicate leftward motion. The black contours in (**b**) show three representative cavitation-bubble shapes.

3.2.3 Phase Diagram of Jet Morphologies

Based on the observed flow fields, we classify the jet morphologies into three distinct types. Fig. 11 presents the classification of bubble jet morphologies under different combinations of non-dimensional distance γ and relative size ratio η. Based on flow-field analysis, three representative jet types are identified: (i) reverse jets (Type I), (ii) opposed jets (Type II), and (iii) co-directional jets (Type III). Here, reverse jets refer to jets that penetrate the cavitation bubble wall on the side away from the air bubble (leftward). Opposed jets are characterized by two counter-directed jets forming inside the cavitation bubble and colliding near its center. Co-directional jets denote jets that are directed toward the air bubble (rightward).

Fig. 11a–c illustrates the evolution processes of three typical jet morphologies. The driving force of the reverse jet (red contour line) mainly comes from the air bubble, which is manifested as a jet that penetrates the bubble wall to the left when the cavitation bubble collapses. The opposed jet (green contour) is simultaneously acted upon by the wall surface of the circular tube and the air bubble, driving the cavitation bubble to collapse and causing two opposing jets to collide within the cavitation bubble. The driving force of the co-directional jet (blue contour line) is dominated by the pressure wave reflected from the wall of the circular tube. Therefore, when the bubble collapses, the jet evolves into a co-directional jet.

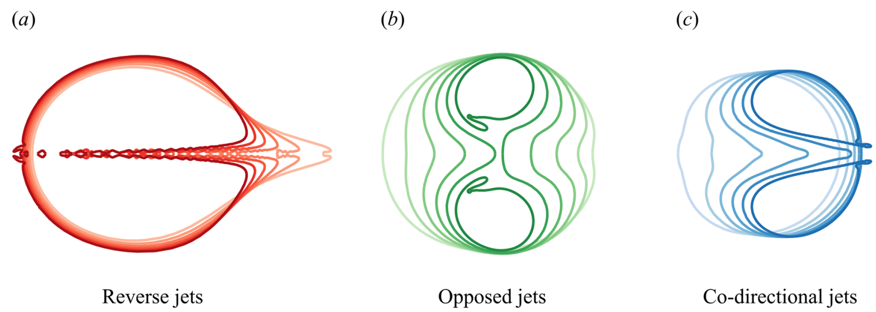

Figure 11: (**a**) Reverse jets (red contours), plotted every 2 μs from 10 μs; (**b**) opposed jets (green contours), plotted every 5 μs from 25 μs; and (**c**) co-directional jets (blue contours), plotted every 5 μs from 30 μs. The contour colors become darker over time.

As shown in Fig. 12, the phase diagram divides the parameter space (γ, η) into three regions corresponding to these jet morphologies. The map shows that the cavitation–air bubble interaction gradually weakens with increasing γ, leading to clear transitions between jet types. For $0.8 < \eta < 1.2$, as γ increases, the bubble interaction changes from strong to weak coupling. At small γ, the cavitation bubble rapidly develops the reverse jets pointing away from the air bubble (Type I). At intermediate γ, the opposing jets appear during the collapse phase, with flows directed toward the interior of the bubble (Type II). At large γ, the cavitation bubble produces co-directional jets oriented toward the air bubble (Type III). For $1.2 < \eta < 1.8$, the air-bubble radius decreases and its surface curvature increases, reducing the effect of the bubble spacing. In this range, opposed jets occur across a wide span of γ values, while co-directional jets emerge at larger γ. When $\eta >$ 2.0, the air bubble is much smaller, and the interaction typically generates reverse jets (Type I) within the cavitation bubble. In summary, the distribution of jet types on the phase map reflects distinct morphological transitions governed jointly by γ and η, illustrating that the jet direction is determined by both the distance between bubbles and their relative size.

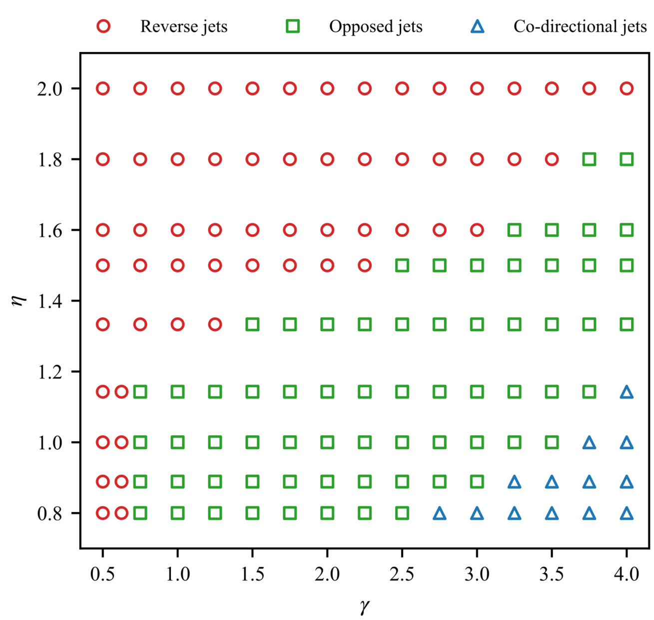

Figure 12: Distribution of jet types in a (γ, η) parametric map. The open symbols denote the computed cases. Circles, squares, and triangles represent reverse jets, opposed jets, and co-directional jets, respectively.

4 Conclusions

In this paper, the cavitation–air bubble interaction inside a rigid circular tube is numerically investigated using a compressible volume-of-fluid method. Two dimensionless parameters are considered: the spacing ratio γ and the size ratio η. The main conclusions are drawn as follows.

The expansion of the cavitation bubble generates a spherical pressure wave. When the wave reaches the tube wall, a high-pressure peak is produced. The pressure waves are reflected at the air-liquid interface, creating a complex localized pressure field. Within the present parameter range and for a fixed tube radius, the peak wall pressure is insensitive to changes in both γ and η. Under different tube radii, a smaller tube radius shortens the propagation distance of the pressure wave, leading to more concentrated energy and a higher peak wall pressure. As the radius of the tube increases, spherical attenuation becomes dominant, and the shock energy is distributed over a larger spatial volume, leading to a significant reduction in the wall pressure amplitude.

Depending on the combination of γ and η, three distinct jetting regimes are identified: reverse jets (Type I), opposed jets (Type II), and co-directional jets (Type III). The phase diagram divides the parameter space (γ, η) into three distinct regions corresponding to these jet types. For $0.8 < \eta < 1.2$, increasing γ weakens bubble coupling, leading to sequential transitions from reverse to opposed and finally to co-directional jets. For $1.2 < \eta < 1.8$, the smaller air bubble suppresses co-directional jets, and opposed jets dominate over a wide range of γ. When $\eta > 2.0$, the air bubble is sufficiently small that reverse jets are typically produced inside the cavitation bubble. The jet direction is therefore governed jointly by the bubble spacing and the relative bubble size.

In summary, the collapse and jetting behavior of a confined cavitation bubble are governed by two competing mechanisms: (i) the wall-reflected pressure impulse that accelerates the liquid toward the air bubble, and (ii) the localized liquid momentum induced by the re-expansion of the adjacent air bubble interface that drives flow in the opposite direction. The interplay between these physical driving mechanisms dictates the final jet regime. The present findings provide insights into cavitation-air bubble interaction under wall confinement, which may be relevant to cavitation control in microfluidic and other confined flow environments.

Acknowledgement: None.

Funding Statement: This research was partly funded by the National Natural Science Foundation of China under grant No. 52371312 and supported by National Key Laboratory of Marine Engine Science and Technology.

Author Contributions: The authors confirm contribution to the paper as follows: writing—original draft preparation: Shiyu Liu; data collection: Shiyu Liu, Bingqi Wang; validation: Shiyu Liu, Bingqi Wang, Jia Liu and Deyu Wang; methodology: Pu Cui; analysis and interpretation of results: Shiyu Liu, Pu Cui, Jiangshan Jin; writing—review and editing: Pu Cui, Jiangshan Jin; project administration: Jiangshan Jin; funding acquisition: Pu Cui. All authors reviewed and approved the final version of the manuscript.

Availability of Data and Materials: The data that support the findings of this study are available from the Corresponding Author, Pu Cui, upon reasonable request.

Ethics Approval: Not applicable.

Conflicts of Interest: The authors declare no conflicts of interest.

References

1. Ma X, Huang B, Zhao X, Wang Y, Chang Q, Qiu S, et al. Comparisons of spark-charge bubble dynamics near the elastic and rigid boundaries. Ultrason Sonochem. 2018;43(1):80–90. doi:10.1016/j.ultsonch.2018.01.005.
2. Aganin A, Kosolapova L, Malakhov V. Bubble dynamics near a locally curved region of a plane rigid wall. Phys Fluids. 2022;34(9):097105. doi:10.1063/5.0105955.
3. Huang J, Zhong Y, Fan Y, Wang J, Wang Y. On the criteria of jet types during a bubble collapse near the tissue-mimicking boundary. Appl Phys Lett. 2025;127(9):092701. doi:10.1063/5.0288620.
4. Wang J, Wen X, Liu K, Jiang M, Wang Z. Experimental study of the motion characteristics of a bubble near a flexible structure with an attached air bubble. Ocean Eng. 2021;235(3):109393. doi:10.1016/j.oceaneng.2021.109393.
5. Wang G, Wang J, Chen X, Huang J, Song G, Zeng Q, et al. Partial ventilation of an oscillating bubble induced by Rayleigh-Taylor instability near a water surface. Phys Rev Fluids. 2025;10(12):123601. doi:10.1103/3q7n-d96f.
6. Bempedelis N, Zhou J, Andersson M, Ventikos Y. Numerical and experimental investigation into the dynamics of a bubble-free-surface system. Phys Rev Fluids. 2021;6(1):013606. doi:10.1103/PhysRevFluids.6.013606.
7. Tagawa Y, Oudalov N, Visser CW, Peters IR, van der Meer D, Sun C, et al. Highly focused supersonic microjets. Phys Rev X. 2012;2(3):031002. doi:10.1103/PhysRevX.2.031002.
8. Zhang AM, Li SM, Xu RZ, Pei SC, Li S, Liu YL. A theoretical model for compressible bubble dynamics considering phase transition and migration. J Fluid Mech. 2024;999:A58. doi:10.1017/jfm.2024.954.
9. Tan Z, Zhang M, Huang G, Huang B. Collapsing behavior of a spark-induced cavitation bubble near the air bubble attached to the tube nozzle. Ocean Eng. 2022;253:111183. doi:10.1016/j.oceaneng.2022.111183.
10. Blake JR, Leppinen DM, Wang Q. Cavitation and bubble dynamics: the Kelvin impulse and its applications. Interface Focus. 2015;5(5):20150017. doi:10.1098/rsfs.2015.0017.
11. Nagargoje MS, Gupta R. Experimental investigations on the bubble dynamics in a symmetric bifurcating channel. Int J Multiph Flow. 2023;159(9):104318. doi:10.1016/j.ijmultiphaseflow.2022.104318.
12. Ren Z, Li B, Xu P, Wakata Y, Liu J, Sun C, et al. Cavitation bubble dynamics in a funnel-shaped tube. Phys Fluids. 2022;34(9):093313. doi:10.1063/5.0107436.
13. Cui P, Wang QX, Wang SP, Zhang AM. Experimental study on interaction and coalescence of synchronized multiple bubbles. Phys Fluids. 2016;28(1):012103. doi:10.1063/1.4939007.
14. Liu S, Wang B, Li SM, Zhang AM, Pu C, Zeng Q. Jet formation in air bubbles induced by cavitation bubbles. J Fluid Mech. 2026;1035:A19. doi:10.1017/jfm.2026.11575.
15. Han B, Köhler K, Jungnickel K, Mettin R, Lauterborn W, Vogel A. Dynamics of laser-induced bubble pairs. J Fluid Mech. 2015;771:706–42. doi:10.1017/jfm.2015.183.
16. Fan Y, Bussmann A, Reuter F, Bao H, Adami S, Gordillo JM, et al. Amplification of supersonic microjets by resonant inertial cavitation-bubble pair. Phys Rev Lett. 2024;132(10):104004. doi:10.1103/PhysRevLett.132.104004.
17. Yin J, Yu Y, Zhang Y, Tian L, Ma M, Huang R, et al. Collapse dynamics and jet transition in the interaction between a near-wall cavitation bubble and a spherical air bubble. Phys Fluids. 2025;37(7):076115. doi:10.1063/5.0276870.
18. Kannan Y, Karri B, Sahu KC. Entrapment and interaction of an air bubble with an oscillating cavitation bubble. Phys Fluids. 2018;30(4):041701. doi:10.1063/1.5025122.
19. Luo J, Xu W, Khoo BC. Stratification effect of air bubble on the shock wave from the collapse of cavitation bubble. J Fluid Mech. 2021;919:A16. doi:10.1017/jfm.2021.368.
20. Wang SP, Wang Q, Zhang AM, Stride E. Experimental observations of the behaviour of a bubble inside a circular rigid tube. Int J Multiph Flow. 2019;121:103096. doi:10.1016/j.ijmultiphaseflow.2019.103096.
21. Yu H, Zhang Y, Zhang X, Sun Y, Liu Y, Yin Z, et al. Dynamic behavior and spatio-temporal mechanical characteristics of the individual cavitation bubble on hydraulic concrete wall. Ocean Eng. 2024;312(2):119197. doi:10.1016/j.oceaneng.2024.119197.
22. Yuan F, Sankin G, Zhong P. Dynamics of tandem bubble interaction in a microfluidic channel. J Acoust Soc Am. 2011;130(5):3339–46. doi:10.1121/1.3626134.
23. Brennen CE. Cavitation in medicine. Interface Focus. 2015;5(5):20150022. doi:10.1098/rsfs.2015.0022.
24. Wang Z, Xu P, Ren Z, Yu L, Zuo Z, Liu S. Dynamics of cavitation bubbles in viscous liquids in a tube during a transient process. Ultrason Sonochem. 2024;104(2):106840. doi:10.1016/j.ultsonch.2024.106840.

25. Wang N, Xu H, Wang T, Che Z. Wall confinement effects on the dynamics of cavitation bubbles in thin tubes. Phys Fluids. 2024;36(4):042101. doi:10.1063/5.0196787.
26. Li JB, Xu WL, Xia Y, Ye M, Zhai YW, Deng J. Effect of an air bubble on the collapse shock wave of a cavitation bubble. Ocean Eng. 2024;297:117094. doi:10.1016/j.oceaneng.2024.117094.
27. Weller HG, Tabor G, Jasak H, Fureby C. A tensorial approach to computational continuum mechanics using object-oriented techniques. Comput Phys. 1998;12(6):620–31. doi:10.1063/1.168744.
28. Zeng Q, Gonzalez-Avila SR, Dijkink R, Koukouvinis P, Gavaises M, Ohl CD. Wall shear stress from jetting cavitation bubbles. J Fluid Mech. 2018;846:341–55. doi:10.1017/jfm.2018.286.
29. Koukouvinis P, Strotos G, Zeng Q, Gonzalez-Avila SR, Theodorakakos A, Gavaises M, et al. Parametric investigations of the induced shear stress by a laser-generated bubble. Langmuir. 2018;34(22):6428–42. doi:10.1021/acs.langmuir.8b01274.
30. Delale CF, Pasinlioğlu Ş. Acoustic cavitation model based on a novel reduced order gas pressure law. AIP Adv. 2021;11(11):115309. doi:10.1063/5.0068152.
31. Brackbill JU, Kothe DB, Zemach C. A continuum method for modeling surface tension. J Comput Phys. 1992;100(2):335–54. doi:10.1016/0021-9991(92)90240-Y.
32. Zeng Q, An H, Ohl CD. Wall shear stress from jetting cavitation bubbles: influence of the stand-off distance and liquid viscosity. J Fluid Mech. 2022;932:A14. doi:10.1017/jfm.2021.997.
33. Koch M, Lechner C, Reuter F, Köhler K, Mettin R, Lauterborn W. Numerical modeling of laser generated cavitation bubbles with the finite volume and volume of fluid method, using OpenFOAM. Comput Fluids. 2016;126:71–90. doi:10.1016/j.compfluid.2015.11.008.
34. Zeng Q, Gonzalez-Avila SR, Ten Voorde S, Ohl CD. Jetting of viscous droplets from cavitation-induced Rayleigh-Taylor instability. J Fluid Mech. 2018;846:916–43. doi:10.1017/jfm.2018.284.